Characterizing Directivity in Small (M 2.4–5) Aftershocks of the Ridgecrest Sequence

Shanna Chu*[1], Annemarie Baltay[2], and Rachel Abercrombie[3]

ABSTRACT

Directivity, or the focusing of energy along the direction of an earthquake rupture, is a common property of earthquakes of all sizes and can cause increased hazard due to azimuthally dependent ground-motion amplification. For small earthquakes, the effects of directivity are generally less pronounced due to reduced rupture size, yet the directivity in small events can bias source property estimates and provide important insights into general regional faulting patterns. However, due to observational limitations, directivity is usually only measured and modeled for large events. As such, many studies of small earthquakes either ignore directivity altogether or assume a constant rupture direction for all events in a cluster. In our study, we apply a refined directivity fitting method constrained with two separate methods of source deconvolution to the dataset of aftershocks of the 2019 Ridgecrest earthquakes, which contain a large number of well-recorded small-to-mid sized earthquakes occurring in close proximity to each other. The revealed directivity of 100+ small (M 2.4–5) earthquakes is highly heterogeneous and primarily oblique to and away from the main fault strike, suggesting a complex postseismic stress redistribution. In addition, the energy focusing effect of directivity appears to bias the selection of high-quality data from stations in the direction of rupture, leading to average stress-drop increases of 50% if directivity is not accounted for.

KEY POINTS

- Directivity is a common feature of earthquakes but difficult to resolve in small events.
- We find highly heterogeneous directivity in small (M 2.4–5) aftershocks of the 2019 Ridgecrest sequence.
- We show that directivity can influence stress-drop measurements and illuminates local faulting complexity.

Supplemental Material

INTRODUCTION

The 2019 M_w 6.4 and 7.1 Ridgecrest earthquakes were the largest seismic events to strike California in over 20 yr (Wang *et al.*, 2020). The M_w 6.4 foreshock, M 7.1 mainshock, and extensive aftershock sequence illuminated a complex multifault network just north of the Garlock fault, highlighting the challenge of understanding seismic hazard in a region with complex fault geometry and a high degree of fault–fault interactions (Ross *et al.*, 2019). The M 7.1 mainshock likely also resulted in stress field adjustment with significant heterogeneity (Sheng and Meng, 2020; Xu *et al.*, 2020), suggesting that regional hazard models may need reassessment.

Rupture directivity, or the focusing of energy in the direction of a propagating earthquake rupture, is a common phenomenon at all earthquake magnitudes and can be especially important for modeling of large earthquake ground motions (Spudich *et al.*, 2013). Directivity has also been extensively observed for smaller earthquakes (Boatwright, 2007; Kane *et al.*, 2013), including induced earthquakes with magnitudes smaller than M 2 (Tomic *et al.*, 2009; Chen *et al.*, 2010; Folesky *et al.*, 2016), but observational resolution generally limits directivity analysis to large, well-recorded (M > 5) earthquakes. If directivity is unaccounted for, it may also cause error in the measurement of rupture-averaged quantities for earthquake source studies, such as stress drop. Combined with the enhanced ground shaking produced in the direction of rupture, it is easy to see why understanding rupture directivity, and whether events in a region have a preferred rupture direction is important for hazards assessment.

Sheng and Meng (2020) previously used a focal mechanism catalog of the Ridgecrest earthquakes to invert for the least complex stress field of the region, showing a small rotation (~5°)

---

1. Department of Earth, Environmental and Planetary Sciences, Rice University, Houston, Texas, U.S.A., https://orcid.org/0000-0001-5974-183X (SC); 2. U.S. Geological Survey, Earthquake Science Center, Moffett Field, California, U.S.A., https://orcid.org/0000-0002-6514-852X (AB); 3. Department of Earth and Environment, Boston University, Boston, Massachusetts, U.S.A., https://orcid.org/0000-0003-4515-5420 (RA)

*Corresponding author: shanna.chu@rice.edu

Cite this article as Chu, S., A. Baltay, and R. Abercrombie (2024). Characterizing Directivity in Small (M 2.4–5) Aftershocks of the Ridgecrest Sequence, *Bull. Seismol. Soc. Am.* **115**, 1177–1188, doi: 10.1785/0120240146

near the M 6.4 foreshock epicenter. Cheng *et al.* (2023) also compiled a refined focal mechanism catalog of Southern California including the Ridgecrest earthquakes using convolutional neural network algorithms, showing a change in faulting style after the main events. However, because events below M ~4 tend to be lacking in certain prerequisites for inversion of rupture direction, such as good azimuthal station coverage and a strong signal in the station-to-station variation of observed earthquake power spectra, very few studies have focused on modeling the directivity of small-magnitude events. Studies of the directivity of small events often leverage constraints on rupture direction, such as the assumption that the rupture direction lies along strike of the single dominant main fault, such as the San Andreas (Kane *et al.*, 2013), or that rupture directions of small earthquakes in a similar tectonic setting are similar and the azimuthal power spectrum can be stacked (Ross *et al.*, 2020). However, directivity has been observed in more heterogeneous faulting settings where it is corroborated by the strikes of natural faults (i.e., Calderoni *et al.*, 2015; Colavitti, *et al.*, 2022) or injection region for the case of induced earthquakes (Folesky *et al.*, 2016). In our study, we examine the Ridgecrest aftershock sequence, which has a highly heterogeneous set of focal mechanism solutions for which the same-direction assumption cannot be made. However, the existence of focal mechanism catalogs provides a point of comparison for directivity models of small events in which the directivity inversion can also help distinguish which nodal plane from the focal mechanism corresponds to the fault plane (e.g., Meng *et al.*, 2020).

DATA AND METHODS

Data preprocessing and source spectrum deconvolution

We use a catalog of events prepared for Ridgecrest Community Stress Drop Validation Study (Baltay *et al.*, 2024; Abercrombie *et al.*, 2024), which is available through the Southern California Earthquake Data Center (SCEDC; see Data and Resources). The dataset and geographic study area are shown in Figure 1. The dataset consists of over 11,000 events over a two-week time period; we refer the reader to Abercrombie *et al.* (2024) for more detailed information about the magnitude–frequency distribution. We use stations from the networks ZY, CI, PB, and GS with channels of the EH and HH format, which are velocity seismometers at a sampling rate of 100 samples per second (Abercrombie *et al.*, 2024; Baltay *et al.*, 2024). The magnitudes of events (hereafter denoted by the single letter M without subscript) refer to the catalog magnitude of the Southern California Seismic Network, which refers to local magnitude below $M_w \sim 3.5$ and M_w above. We refer the reader to Gable and Huang (2024)and Baltay (2024) for additional discussion about the effects of the choice of magnitude scale.

For each event, we limit the maximum distance of stations to 100 km from the event epicenter, consistent with the common dataset distributed as part of the community study. We use S-wave data from the station horizontal channels, cut to window lengths of min(4 s, $10 \times \tau$). Here, τ denotes the source duration, for magnitudes less than M 3.0 and min(6 s, $10 \times \tau$) for magnitudes greater than M 3.0 for which the expected source duration was estimated from a constant Brune stress drop of 2.4 MPa (computed for the region by Trugman, 2020). The data are then band-pass-filtered between a magnitude-dependent low-cut frequency and 40 Hz (see Text S1, available in the supplemental material to this article, for additional details on calculation of source duration and the band-pass filter).

The demeaned, detrended data are converted to the frequency domain using the multitaper method (Prieto, 2022) and resampled to 101 evenly log-spaced points. We retain all events with signal-to-noise ratio (SNR) greater than 3. For the SNR calculation, data are across 10 log-spaced frequency bands from 1 to 40 Hz, and data are sampled from the signal window are compared to a noise window of the same length ending 0.5 s before the P-wave arrival. We then apply the spectral ratio method (e.g., Mori and Frankel, 1990; Imanishi and Ellsworth, 2006; Abercrombie, 2021) to deconvolve the spectrum due to the earthquake source for a number of target events within our set of processed spectra. With this approach, a small event, ideally with a rupture dimension not resolvable within observational bandwidth, will serve as an "empirical Green's function" (eGf) for a larger event of interest, whereby the path and site effects are expected to be the same as those for the target event (Hartzell, 1978; Hough, 1997), and can be removed via time-domain decomposition or frequency-domain spectral division,

$$\frac{S(f)}{S_{\mathrm{eGf}}(f)} = \frac{\Omega(f) \times I_j(f) \times P_k}{\Omega_{\mathrm{eGf}}(f) \times I_j(f) \times P_k}, \tag{1}$$

in which S, S_{eGf} are the observed Fourier amplitude spectra for the target event and eGf respectively, I_j and P_k are common site response and path terms that are canceled out upon spectral division, respectively, $\Omega(f)$ represents the true event source spectrum. The resulting ratio of the two spectra will have a corner frequency related to the characteristic source dimension of the larger event's ruptured fault, beyond which the spectral power falls off. The exact shape of the power spectrum is dependent on factors such as the source pulse and fault geometry (e.g., Boatwright, 1980) and may be approximately described by a number of analytical source models. Here, we use a Brune (1970) spectral model to fit the corner frequency in ratio form,

$$\frac{\Omega(f)}{\Omega_{\mathrm{eGf}}(f)} = \frac{M_0(1 + (f/f_{c,\mathrm{eGf}})^{n\gamma})^{1/\gamma}}{M_{0,\mathrm{eGf}}(1 + (f/f_c)^{n\gamma})^{1/\gamma}}, \tag{2}$$

in which M_0, $M_{0,\mathrm{eGf}}$ and f_c, $f_{c,\mathrm{eGf}}$ represent the moment and corner frequency of the target event and eGf, respectively, and the parameters $n = 2$, $\gamma = 1$ are model-dependent terms controlling the rate of high-frequency spectral fall off and its

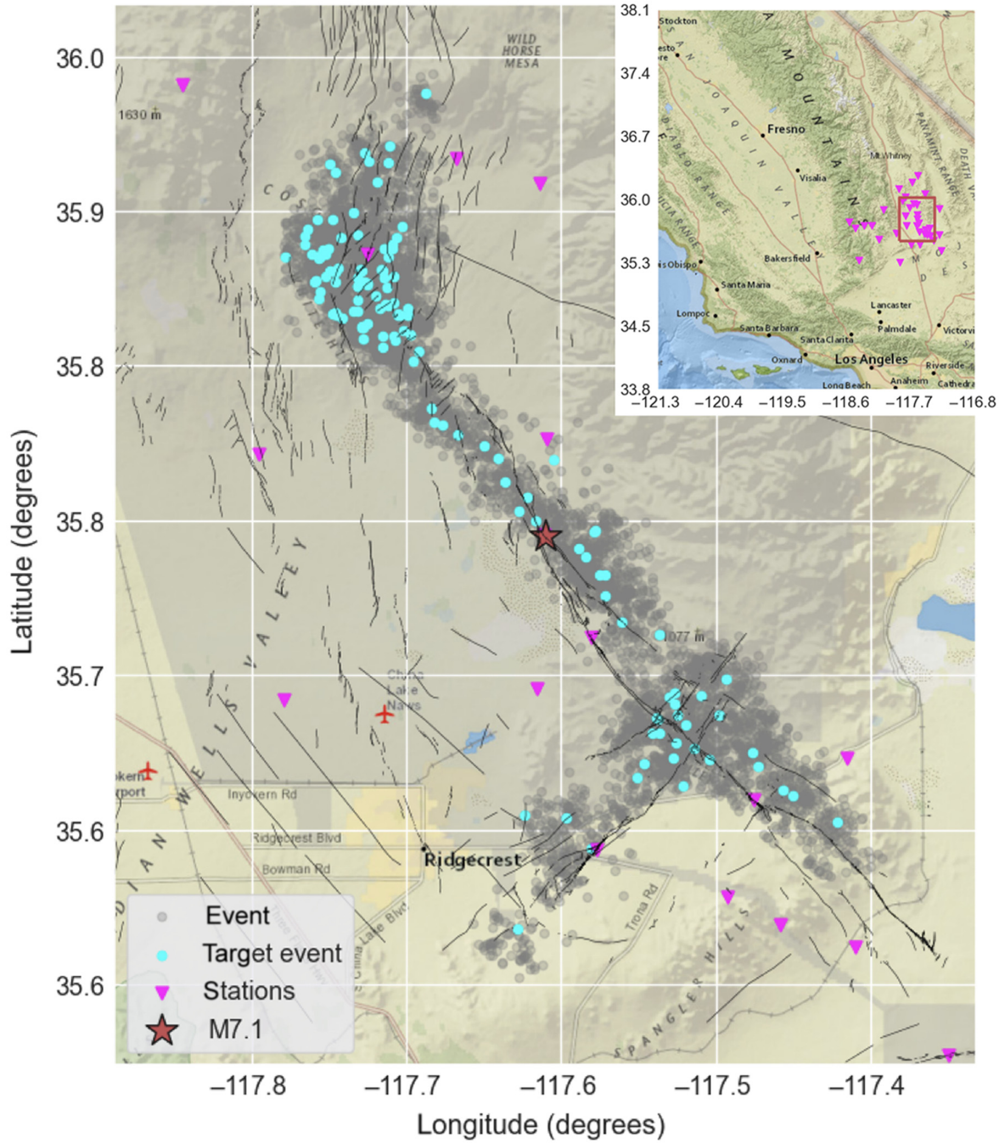

Figure 1. The target events, empirical Green's function (eGf) events used in spectral ratio analysis, and stations used in this study. Mapped faults are shown as thin black lines, and the epicenter of the M 7.1 mainshock is denoted by a red star. The inset shows the study area (in a red box) within the general location in Southern California, north of Los Angeles. Additional stations too far to be shown clearly in the main plot are also shown in the inset. Map tiles are retrieved from Environmental Systems Research Institute (Esri) and National Geographic via the ArcGIS online server. The color version of this figure is available only in the electronic edition.

sharpness, respectively. An ideal candidate for a suitable eGf is one with similar hypocentral location and a high-waveform cross correlation with the target event of study. We estimate source radii for target events, again assuming a constant Brune stress drop of 2.4 MPa, and choose eGf events within five times this estimated source radius, which ensures a good balance of sufficient eGf events and eGf-target event similarity. The eGf candidates are cross-correlated in the frequency range filtered below an estimated f_c of the target event (from the same constant stress drop of 2.4 MPa), and, following Abercrombie *et al.* (2017), candidates which had a waveform cross correlation of at least 0.7 with the target event are retained. Although Abercrombie (2015) suggests using eGfs located within one source radius of the target event to avoid biases, we found that restriction yielded too few eGf candidates for stable f_c estimates and too few stations for azimuthal coverage when performing the directivity analysis. After obtaining spectral ratios, we discard those spectral ratios for which the amplitude ratio of the low- to the high-frequency asymptotes was greater than 10 following Chu *et al.* (2019) and Abercrombie (2014) to ensure that the resulting spectral ratios are sufficiently Brune-like.

For a station-event pair to be included in our study, we require them to have spectral ratios from at least eight different eGf events at a station. In addition, each event needs to be recorded on at least eight stations with sufficient eGf count. We constrain the allowable station distance as per Seekins and Boatwright (2010) to retain primarily upgoing *S*-wave takeoff angles, based on event depth. After all constraints are applied, we have a total of 545 events between M 2.0 and 5.5. The effective maximum station-to-event distance for this selection ranges from a maximum of 40 km for M 2.5 earthquakes to 80 km for M 5 earthquakes. Because we are interested in observing station-to-station azimuthal variations in estimates of the f_c, we fit f_c at each station to minimize the total (global) misfit to all eGf spectral ratios using L1 regression with a smoothed loss function (Huber, 1964; Charbonnier *et al.*, 1997), which is robust to outliers. An example of spectral ratios modeled at different stations for a single event is shown in Figure 2.

Directivity modeling

Directivity can be resolved when the station coverage of an event sufficiently resolves the variation in observed apparent f_c, source duration, or wave amplitude (e.g., Boatwright, 2007; Prieto *et al.*, 2017; Van Houtte and Denolle, 2018;

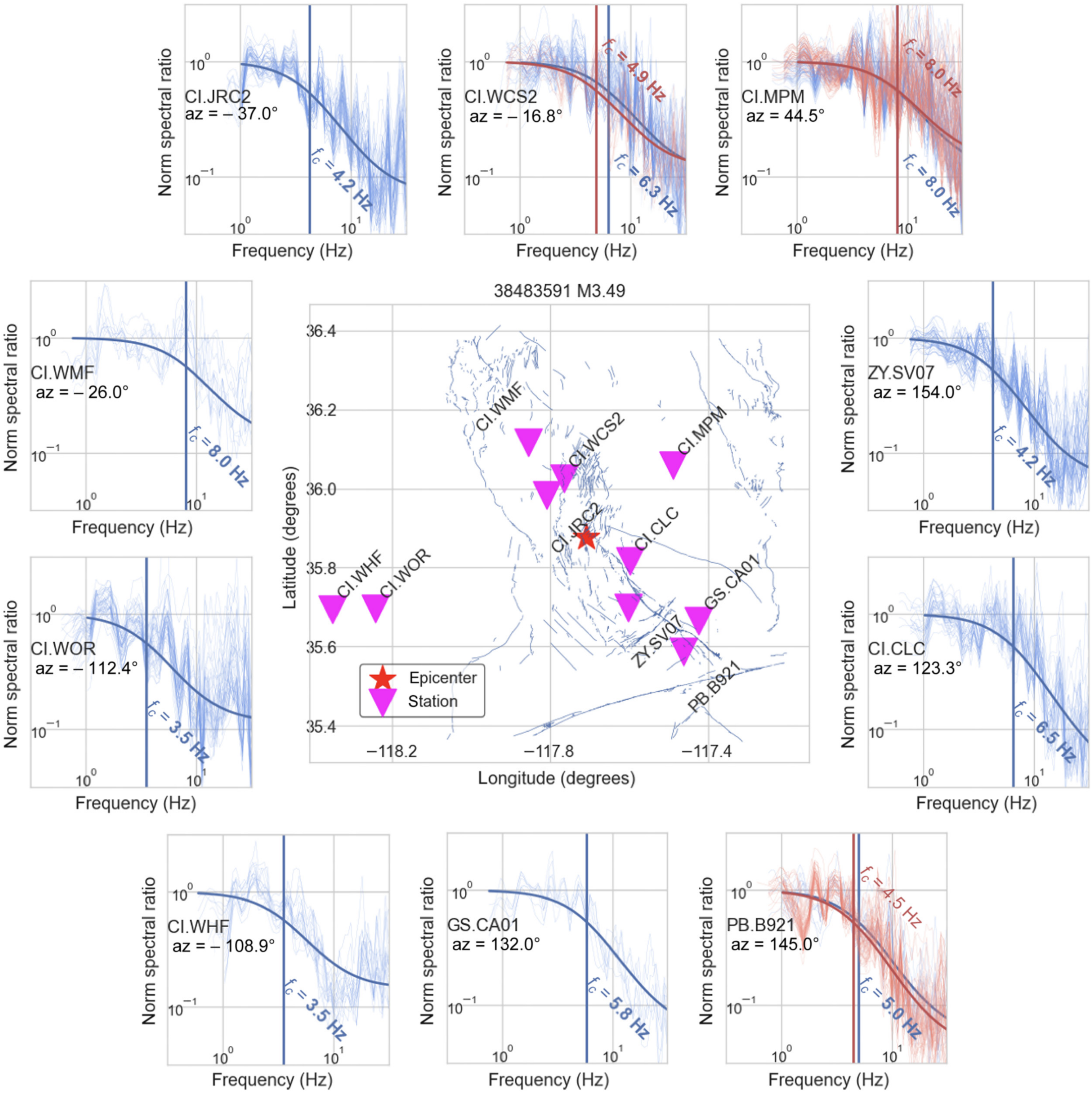

Figure 2. Example of station-to-station azimuthal fits of corner frequency for event 38483591 (M 3.49). Fits of different color indicate separate fits for individual station components. Fitting is performed separately because we did not retain records at both components for all stations after selection for data and eGf quality. Azimuthal spectral ratios are shown with normalized amplitudes and roughly corresponding to their map location, shown in the central subplot, for which the red star denotes the event epicenter and thin lines indicate the mapped faults. The color version of this figure is available only in the electronic edition.

Trugman, 2022). (We note thus that the variations in source duration of the events used as eGfs will generally not be resolvable due to their extremely short duration, so we do not consider the eGf events themselves to have directivity in our study). We choose to model variability in f_c here because we find that this is the best-constrained metric from the eGf spectral ratio method, in which f_c is better resolved than amplitude. Here we briefly outline other methods, such as variability in normalized spectral amplitude (Ross and Ben-Zion, 2016) and energy amplitude variation using spectral decomposition (Ross *et al.*, 2020). We find that these methods correlate well with the f_c variation method but yield greater scatter (Fig. S1). Another method to measure directivity is inversion for the second moment (McGuire, 2017), which relies on apparent source time functions (ASTFs) obtained from the

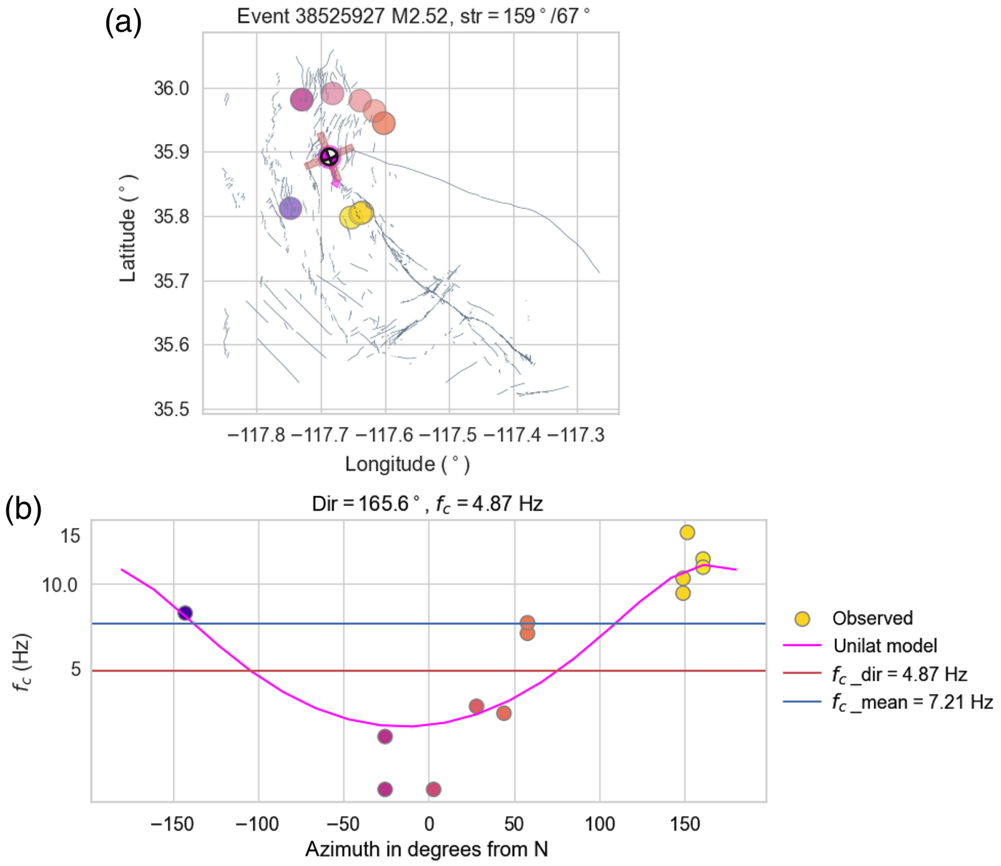

Figure 3. A sample fit of station-to-station corner frequency variation for a unilaterally directive event. The strike direction from the focal mechanism is 159° or 67° as shown in the focal mechanism plot in panel (a), with a fitted rupture direction of 165.8°. Dots surrounding the focal mechanism plot denote the location of the stations used in the analysis and are colored by azimuth. The corner frequency when accounting for directivity is 2.34 Hz lower than the averaged corner frequency, as shown in the fit in panel (b). The *x* axis in panel (b) measures azimuth from due north. The color version of this figure is available only in the electronic edition.

Projected Landweber deconvolution (Bertero *et al.*, 1997). We found that this method works best with well-constrained known focal mechanisms and clear arrivals for both a target and eGf event, which are manually windowed. We were able to fit fewer events using second moment inversion, but the directivity results are similar to our results for these events from corner frequency inversion (Fig. S2, Table S1).

To fit a directivity model to each of our events, we require a maximum azimuthal gap in the station coverage of less than 40% of the unit circle (144°), reducing the number of usable events to 171. The variation in apparent corner f_c is fitted to one of two models, one which accounts for the possibility of bilateral rupture (Boatwright, 2007) and one which does not. Simple unilateral directivity in a horizontal plane is modeled as

$$f_{c,j} = f_c \frac{1}{1 - (v_r/\beta)\cos\theta}, \qquad (3)$$

in which $f_{c,j}$ is the apparent corner frequency as a function of azimuth (at station j), f_c is the true corner frequency, v_r and β are the rupture velocity and shear-wave speed, respectively, which in practice are fit as a ratio, and θ is the azimuthal angle between rupture direction and station azimuth. The more general formulation of directivity considering the possibility of bilateral rupture and event depth (e.g., Boatwright, 2007; Trugman, 2022) is given as

$$f_{c,j} = D_j f_c,$$
$$D_j \sim \frac{[(1+e^2)(1+\varsigma_j^2) + 4e\varsigma_j]^{1/2}}{\sqrt{2}(1-\varsigma_j^2)}, \qquad (4)$$

in which $\varsigma_j = \frac{v_r}{\beta}\cos\theta_j$ and $\cos\theta_j = \cos(\varphi_r - \varphi_j)\sin\phi_r\sin\phi_j + \cos\phi_r\cos\phi_j$ is a function of both the horizontal azimuth φ and takeoff angle ϕ computed from the velocity model of White *et al.* (2021). Subscripts r refer to rupture directions whereas j refers to the angles of stations. The parameter e, also called the directivity ratio (McGuire *et al.*, 2002; McGuire, 2004), tends to 0 for true bilateral rupture and 1 for true unilateral rupture. The full directivity model increases the number of fitted parameters from three to five. We evaluate each directivity fit using three models: a horizontally unilateral model (equation 3); a full model, inverting for takeoff angle and the possibility of bilateral rupture (equation 4); and, a mean average f_c as a null hypothesis for no directivity. Then, the Akaike information criterion (AIC; Akaike, 1974; Burnham and Anderson, 2003; Text S2) is calculated for each model to select the most likely model given the data. Figure 3 shows a sample station-to-station fit of azimuthal f_c for the simple directivity model (equation 3). An analogous example fit using the full directivity model (equation 4) is shown in Figure S3; the large number of parameters in this model makes it less straightforward to display on a 2D plot.

RESULTS

Directivity of Ridgecrest aftershocks

From our directivity fitting, we separate events into those that are more likely unilaterally directive, bilaterally directive, and events where directivity models did not yield a significantly better AIC than the null hypothesis (Fig. 4a,b). For events for which the best-fitting model was the full directivity model,

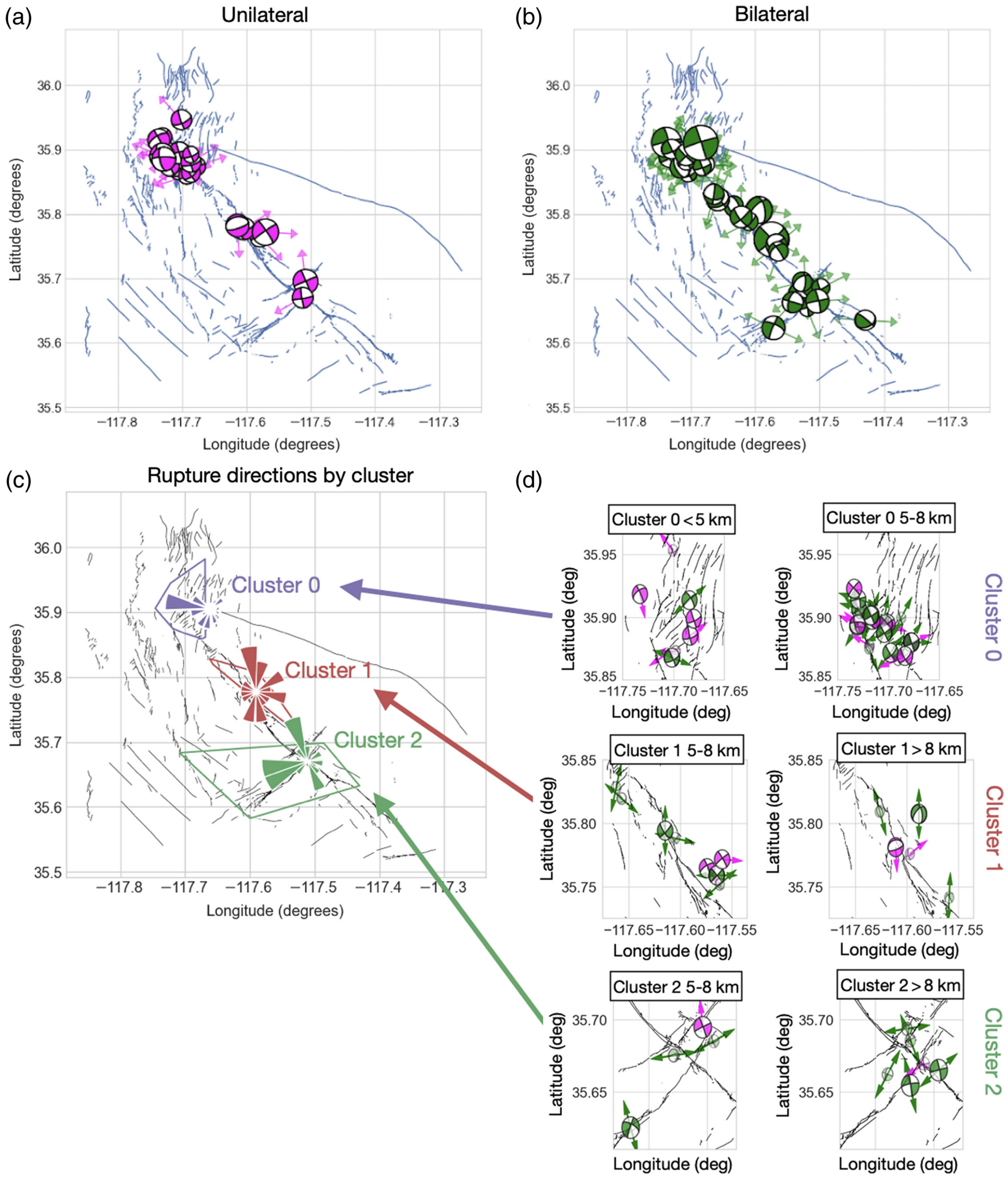

Figure 4. Overlain focal mechanisms of Cheng *et al.* (2023) with the events used in this study for which unilateral or bilateral directivity could be resolved. The events appear to be clustered in three regions, for which convex hulls are shown in panel (c): the northern region along an area of parallel faults, the middle region, and the southeast region near the main orthogonal cross-cutting fault. The general sense of rupture directions (for all types of directive ruptures) is also shown in panel (c), and tends to be heterogeneous. It appears to be mostly oblique to the main northwest–southeast-trending fault particularly in the central and southeast cluster. Along the northern region of parallel fault strands, the general trend of rupture directivity is somewhat rotated and aligned with mapped faults. Panel (d) shows close-ups of each cluster, separated by depth. Focal mechanisms (from the Cheng *et al.*, 2023 catalog) with (c,d) lower quality are shown with smaller focal mechanism plots than (a,b) higher quality ones. The northernmost cluster (cluster 0), for which events show the greatest degree of alignment with surficial fault traces, is also the only cluster with events in the upper 5 km (note the depth of events shown ranges from 0 to 8 km for cluster 0 and from 5 to 8+ km for clusters 1 and 2). Events at middle depths in cluster 0 appear to be more tightly clustered and possibly show more westward-trending ruptures, unlike the surficial faults and events. The color version of this figure is available only in the electronic edition.

the event was labeled as unilaterally directive if the directivity ratio, $e > 0.6$ and bilateral if $e < 0.4$. The 133 events out of the tested 545, shown in Figure 4, were fitted to a unilateral or bilateral model over the null hypothesis; there is not a clear spatial pattern in where unilateral or bilateral rupture is observed. In practice, the fitted rupture directions of the full directivity model with $e < 0.4$, and the simple unilateral directivity model often yielded similar results, and previous authors have shown that unilateral rupture and asymmetric bilateral rupture are often difficult to distinguish (Dempsey and Suckale, 2016; Abercrombie *et al.*, 2017), especially given that our station distribution is often less than ideal. Therefore, our results should not be taken to indicate a preference for the unilateral or bilateral rupture amongst the Ridgecrest aftershocks, but a more general indicator of directivity.

It is not surprising that the limit of resolving station-to-station directivity appears to be controlled by event magnitude, as smaller events with shorter source–time durations are less likely to have resolvable variability in f_c from station to station and may also have lower data quality or number of stations, leading to poorer constraints in fitting. In our dataset, there appears to be a magnitude cutoff for observable directivity in our dataset at around M 2.2, which is a similar limit to what has been found in some previous studies (Abercrombie *et al.*, 2020; Pennington *et al.*, 2023). Because the variation in apparent source duration and corner frequency of small events is difficult to resolve with bandlimited seismic data, we note that this resolution limit does not exclude there being real directivity effects in events below M 2.2. The heterogeneous rupture directions of the aftershocks tend to run orthogonal to the main fault of the mainshock, but show no strongly preferred rupture direction. However, there is some spatial variation in rupture direction: Figure 4c shows the average trend of fitted rupture direction separated into three spatial clusters, visually separated by latitude. In particular, the northernmost cluster, which also had the most fit events, appears to have a preferred rupture direction to the west. The northern cluster also contains the shallowest events (<5 km deep, Fig. 4d), with the shallowest events being more spatially spread out than the deeper ones below 5 km. In addition to the west-trending events, which tend to occur at the southern edge of the northern cluster, there is a subtrend of events with northeast–southwest-trending ruptures, somewhat aligned to the direction of the mapped semiparallel surface fault strands.

Effect of directivity on measured stress drop

To better understand Ridgecrest aftershock directivity and its effect on stress-drop fitting, we further limit our analysis to those events with strike-slip focal mechanisms, defined as having a scalar focal mechanism with absolute value less than 0.33. The scalar focal mechanism is computed from the rake as in Shearer *et al.* (2006) and varies between −1 (normal faulting) and 0 (strike slip) and 1 (reverse faulting). Focal mechanisms are provided by the catalog of Cheng *et al.* (2023). Out of the 133 events with apparent directivity, we selected 39 strike-slip events within 30° of the published catalog nodal planes, which is within the uncertainty range for the higher quality focal mechanism inversions (25°–35°, respectively, for "A" and "B" quality focal mechanisms) from the catalog. The fitted rupture directivity can thus be used to constrain which of the two nodal planes from the focal mechanism solution is more likely.

A key scientific question raised in the articles of this volume is which factors contribute to the variability of the measured stress drop. In our study, we measure the effect of directivity. To understand its isolated effect on stress drop, we fit stress drop using the Brune (1970) model,

$$\Delta\sigma = \frac{7}{16} M_0 \left(\frac{f_c}{k_s \beta}\right)^3, \tag{5}$$

in which M_0 is seismic moment estimated from the moment magnitude, f_c is the fitted corner frequency, β is shear-wave speed from the velocity model of White *et al.* (2021), and $k_s = 0.26$ under the assumption that the rupture velocity is 0.9 times the shear-wave speed (Kaneko and Shearer, 2014). The full catalog of calculated stress drop results from our analysis, including a complementary method using spectral decomposition, are also published in a companion article in this issue (Abercrombie *et al.*, 2024). Among the 39 selected strike-slip events, eight of the small events showed unreasonably high stress drops (>100 MPa) and seven showed very low ones (<1 MPa), indicating the effect of possibly unaccounted-for high-frequency effects or the effect of approaching the high end of observable bandwidth. We remove these outliers resulting in 24 high-quality events.

Stress-drop fitting using the spectral ratio method as described in this article is often averaged over stations and assumes that the stations used in the dataset have good azimuthal coverage. Figure 5a shows the calculated stress drops of the same set of 24 analyzed strike-slip events, both by the common method of averaging over stations and directly inverting for rupture direction. Even by analyzing the stress drops using the exact same processing method, inverting for the directivity-corrected f_c yields an average stress drop that is lower by about ∼4.3 MPa or about 50%.

DISCUSSION

Effect of directivity on stress-drop measurements

Although directivity can be difficult to measure in the case of small-magnitude events with limited station coverage, our study shows that it can have appreciable effect on the station-to-station measurement of corner frequency and stress drop. Although we can indeed determine meaningful directivity solutions for a number of events that are supported by previously published focal mechanisms, the primary aim of the article is not to constrain the exact rupture direction for each small event but rather to show the regional trend and the effect directivity has on

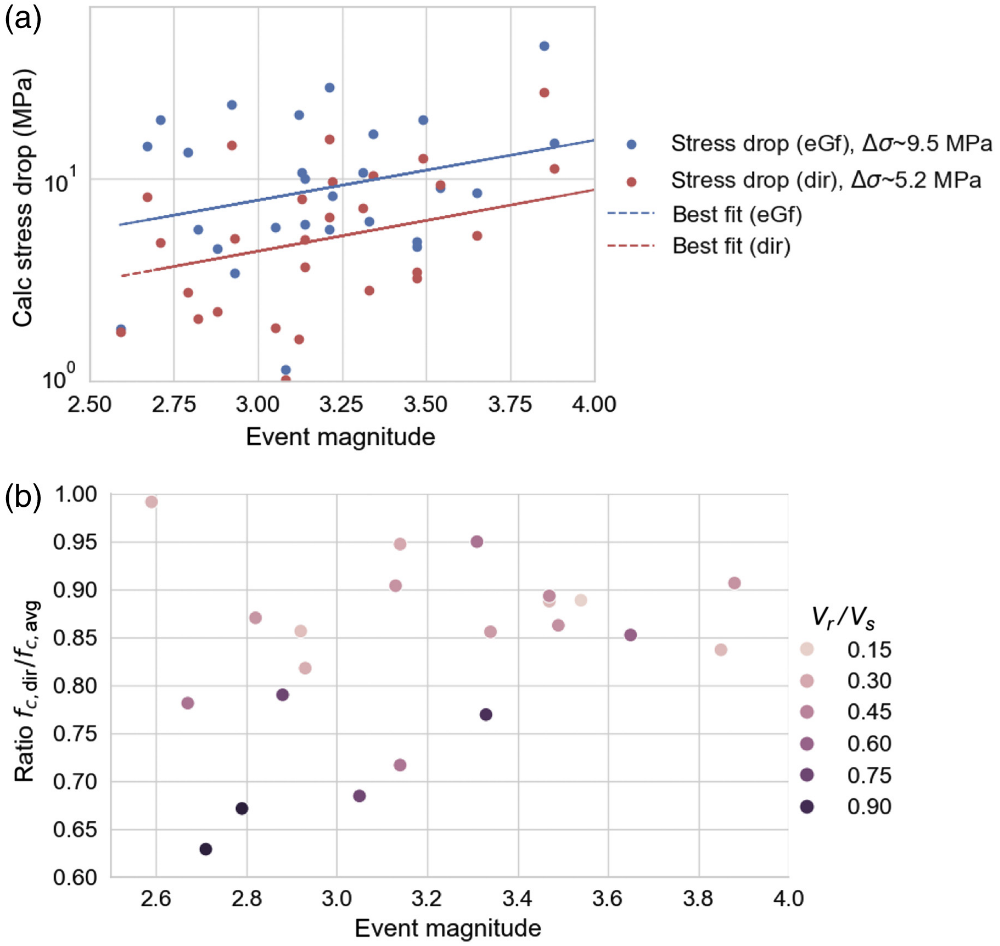

Figure 5. (a) Stress drop estimated using the Brune (1970) model with and without adjustment to the corner frequency from directivity. The median decrease in stress drop when directivity is accounted for is around 4.3 MPa or 50% of the estimated stress drop. However, the general trend in the stress drops can be seen to be the same, indicating that directivity has the effect of systematically shifting measured stress drop to higher values. There is no obvious scaling of stress drop with magnitude. (b) The average ratio of the corner frequencies after accounting for directivity is roughly 80%–90% of the non-adjusted corner frequency without a significant dependence on event magnitude. However, rupture velocity is likely underestimated across all directivity fits, due to the effect of a limited frequency band of observation. The color version of this figure is available only in the electronic edition.

source measurements. The findings have twofold implications: (1) the effect of directivity alone can bias stress-drop estimates up to 50% even with all other processing steps being equal and (2) the heterogeneity of rupture direction amongst Ridgecrest aftershocks indicates a complex fault network.

To further probe why directivity could have the effect of increasing average measured stress drop, we analyze the effect of station distribution. We look at the number of included stations in each azimuth bin overlain over the number of total stations at which data for the studied events were available (Fig. 5a), and Figure 5b shows the same information as a percentage (an example for a single event located in the middle of the study area is shown in Fig. S4). Although the layout of stations in the Ridgecrest region trends predominantly in the northwest–southeast direction, the stations that were selected for data SNR quality have somewhat of a mixed trend, with a large proportion of selected stations being in the northeast–southwest direction, orthogonal to the fault segment rupturing in the mainshock. We also consider the station direction as a function of angular distance from inverted rupture direction (Fig. 6c,d). From this we can see that there is a slight increase in the percentage of stations used that lie close to the rupture direction between 0° and 45° (Fig. 6d), suggesting that energy focusing along the rupture direction can produce stronger signals and hence a station selection bias. Bilateral rupture may account for the slight increase in station usage opposite to the rupture direction. On the other hand, there is a slight decrease in the percentage of stations in the orthogonal direction to rupture (~90°). The different distribution of the selected stations compared to the distribution of the true ones indicates a possible biasing effect of directivity to produce stronger signals in the direction of rupture for which the ASTF is shortened, resulting in higher measured stress drops. We note that the results from spectral decomposition, which are not further discussed in this article but are shown in a companion article of this volume (Abercrombie *et al.*, 2024), show a similar median to the stress drops from corner frequencies of the spectral ratio method not considering directivity, as spectral decomposition methods (such as the generalized inversion technique) tend to ignore azimuthal path effects (Fig. S5). However, the other methodological differences between the spectral ratio and spectral decomposition methods extend beyond the scope of this article.

Furthermore, we would expect that the degree to which an event is directive will influence the degree to which stress drop is overestimated; indeed, past studies show that station-to-station variation of measured corner frequency can be greater than a factor of 4 (Holmgren *et al.*, 2019). The ratio between the averaged corner frequencies of the events with and without

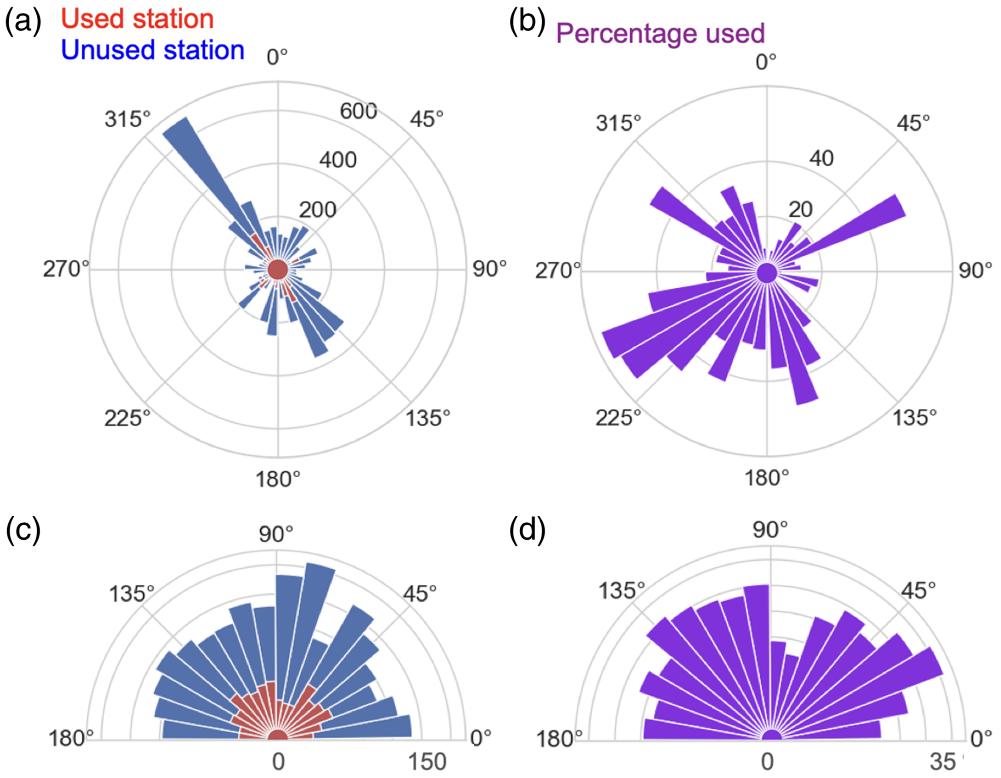

Figure 6. Histograms of summed station azimuths for all events both as a regional angle (from due north, in panel a) and as a function of difference from the fitted rupture direction (c). See Figure S4 for a similar plot of a single event. The used stations are plotted in red over the full set of stations used (and therefore represent a percentage). The same information is plotted as percentages in panels (b) and (d). There appears to be a trend for which the azimuths of stations used for spectral ratio fitting are not correlated to the highest geographic density of stations, suggesting that station selection may instead be biased toward rupture direction. Panel (d) shows a slight increase in the percentage of stations used within 45° of the fitted rupture direction, whereas there is a decrease in the percentage of stations used at 90°. The color version of this figure is available only in the electronic edition.

accounting for directivity ($f_{c,\mathrm{dir}}/f_c$) is dependent on both magnitude and v_r/c, the ratio of rupture velocity to shear-wave speed (Fig. 5b, Fig. S6). Because the azimuthal variation in apparent source duration will become more noticeable at higher rupture velocities (and large magnitudes), we see that our expectation is justified: events with faster rupture velocity show a greater relative difference between averaged f_c and "true" f_c estimated from the directivity model.

However, some of the fit rupture velocities are anomalously low, given that stress drop is usually fit in most studies assuming $v_r/c = 0.9$. The average v_r/c fitted is approximately 0.5, in which case, following the models of Kaneko and Shearer (2014), we should use $k_s = 0.22$ in the stress-drop calculation instead to account for low rupture velocity. This would interestingly lead to true stress drops closer in value to the ones estimated by simply averaging over all corner frequencies but would have different physical implications, given a low rupture velocity (Fig. S7). Another plausible cause of the low fit rupture velocity is the effect of the limited frequency band of observation (1–40 Hz), which may have the effect of reducing the apparent station-to-station variability in observed f_c. Given that the events with v_r/c that are closer to 0.9 tend to have relatively lower corner frequencies and stress drops compared to the station-by-station averaged values, limitation of the frequency bandwidth may likely mean that we are overestimating the stress drop even more in these cases. We find the effect of limited bandwidth a more plausible explanation for the fitted low rupture velocity because it has been confirmed in previous studies with data and synthetic testing (Abercrombie *et al.*, 2017). As such, the rupture velocity will be poorer constrained compared to the rupture direction (which is constrained by the locations of peaks and troughs rather than amplitude), and we obtain artificially slow rupture velocities. We do not notice a significant trend in the fit ratio between rupture velocity and shear-wave speed v_r/c, and the fit ratio between the directivity-corrected corner frequency and the station-averaged corner frequency, $f_{c,\mathrm{dir}}/f_{c,\mathrm{avg}}$. This suggests that as long as the event's true corner frequency lies well within the frequency band of observation with enough azimuths at which the pattern of variation can be observed, the rupture direction and true corner frequency are well-constrained at the expense of poorly constrained rupture velocity (Fig. 6b).

Heterogeneous rupture directions of aftershocks

The observed directivity of the Ridgecrest aftershocks is highly heterogeneous with no distinct trends in any direction, except that the general trend of aftershock directivity tends to be oblique to the primarily northwest-striking fault segments that ruptured during the M 6.4 and 7.1 events preceding (see e.g., Wang *et al.*, 2020). Seismic tomography (Zhou *et al.*, 2022) and modeling of mapped ruptures (Nevitt *et al.*, 2023) indicate that the region near the M 7.1 event rupture area is surrounded by a damage zone with distributed faulting, possibly reactivated from previous seismicity. As such, the high variability we see here in rupture directivity may be representative of an immature fault network with a heterogeneous stress field.

There is as mentioned, some spatial variability: the northernmost cluster of events shows some preference for ruptures trending not only mostly west but also partially northwest–southeast, aligning with surficial mapped faults. High-resolution fault imaging (Qiu *et al.*, 2021) shows cross-fault velocity contrasts in the Ridgecrest mainshock region (south of the northern cluster), possibly indicative of bimaterial structure. The prevalence of bimaterial structure throughout our study area is not well-constrained. It is possible that elastic contrast due to bimaterial structure may influence preferred rupture direction in the northernmost cluster, but it is debatable to what depths this contrast could control rupture direction or whether rupture direction is controlled predominantly by other factors such as fault segment interactions or local stress conditions (Andrews and Harris, 2005).

Chu *et al.* (2021) also found that the northernmost region of Ridgecrest to have the lowest metric of misalignment, or fault network complexity, associated with lower measured stress drops. Fault network complexity and its correlation with elevated stress drops have implications for hazards (see the aforementioned article, and also Chatterjee *et al.*, 2024). Our study shows how understanding regional trends in directivity is important in illuminating this complexity. Furthermore, although directivity effects may bias estimates of true crustal stress drops, they may represent true hazards from the perspective of energy focusing and enhanced ground motions, and can also affect interpretations of other path or site parameters (e.g., Hirakawa *et al.*, 2023).

CONCLUSION

We explore directivity of aftershocks of the 2019 Ridgecrest events with magnitudes 2.4–5 in a two-week period as part of the Southern California Earthquake Center/U.S. Geological Survey (SCEC/USGS) Ridgecrest Community Stress Drop Validation project (Baltay *et al.*, 2024). We find that many of these events exhibit a noticeable station-to-station variation in corner frequency which we use to invert for rupture direction. The fitted rupture directions exhibit a great deal of complexity, generally oblique to the main northwest–southeast-trending nature of the main rupture, although the northern region tends to have more southeast-rupturing events. This is consistent with findings from tomography and fault mapping studies indicating local geologic complexity and stress heterogeneity.

We also find that the general effect of estimating stress drops without fully accounting for directivity has the effect of biasing stress-drop estimates to higher values by up to 50%. Biases due to neglecting directivity is expected, but the fact that it biases to higher values is interesting. This is possibly attributed to the selection bias of high-SNR stations in the direction of rupture propagation. Measured stress drops are used in different ways: for example, in ground-motion analysis, rupture directivity causing enhanced ground motion in one direction is a useful physical parameter rather than an ambiguous one. As such, our findings suggest that as seismic networks improve, understanding the directivity effects of small events will become an important consideration in future stress-drop studies.

DATA AND RESOURCES

All data used for this study were obtained from the Southern California Earthquake Data Center (SCEDC), curated for the Technical Activity Group (https://scedc.caltech.edu/data/stressdrop-ridgecrest.html). Other relevant data available at https://server.arcgisonline.com/ArcGIS/rest/services/. Both websites were last accessed in September 2024. The supplemental material includes additional text (S1–S2) with methodological details, fitted directivity models and their description (text S3), 5 additional figures, and 1 table.

DECLARATION OF COMPETING INTERESTS

The authors acknowledge that there are no conflicts of interest recorded.

ACKNOWLEDGMENTS

The authors thank Y. Y. Lin, J. McGuire, and H. Meng for useful comments, as well as L. Colavitti, R. Skoumal, and an anonymous reviewer who have greatly helped to improve the article. S. Chu graciously acknowledges support from the U.S. Geological Survey (USGS), Southern California Earthquake Center (SCEC), and Pacific Gas & Electric Company. This research was supported by Statewide (previously Southern) California Earthquake Center Awards 21083, 21114, 22101, 22042, 23107, and 23108. SCEC is funded by the National Science Foundation (NSF) Cooperative Agreement EAR-1600087 and USGS Cooperative Agreement G17AC00047. Any use of trade, firm, or product names is for descriptive purposes only and does not imply endorsement by the U.S. Government.

REFERENCES

Abercrombie, R. E. (2021). Resolution and uncertainties in estimates of earthquake stress drop and energy release, *Phil. Trans. Roy. Soc. Lond. A* **379,** 20200131, doi: 10.1098/rsta.2020.0131.

Abercrombie, R. E. (2015). Investigating uncertainties in empirical Green's function analysis of earthquake source parameters, *J. Geophys. Res.* **120,** 4263–4277, doi: 10.1002/2015JB011984.

Abercrombie, R. E. (2014). Stress drops of repeating earthquakes on the San Andreas Fault at Parkfield, *Geophys. Res. Lett.* **41,** 8784–8791, doi: 10.1002/2014GL062079.

Baltay Sundstrom, A. S., R. E. Abercrombie, S. X. Chu, and T. Taira (2024). The SCEC/USGS community stress drop validation study using the 2019 Ridgecrest earthquake sequence, Seismica, doi: 10.26443/seismica.v3i1.1009.

Abercrombie, R. E., X. Chen, and J. Zhang (2020). Repeating earthquakes with remarkably repeatable ruptures on the San Andreas Fault at Parkfield, *Geophys. Res. Lett.* **47,** e2020GL089820, doi: 10.1029/2020GL089820.

Abercrombie, R. E., P. Poli, and S. Bannister (2017). Earthquake directivity, orientation, and stress drop within the subducting plate at the Hikurangi margin, New Zealand, *J. Geophys. Res.* **122,** 10,176–10,188, doi: 10.1002/2017JB014935.

Akaike, H. (1974). A new look at the statistical model identification, *IEEE Trans. Autom. Control* **19,** no. 6, 716–723, doi: 10.1109/TAC.1974.1100705.

Andrews, D. J., and R. A. Harris (2005). The wrinkle-like slip pulse is not important in earthquake dynamics, *Geophys. Res. Lett.* **32,** L23303, doi: 10.1029/2005GL023996.

Baltay, A. S. (2024). Southern California moment and magnitude scales from the SCEC/USGS community stress drop validation study (submitted).

Baltay, A. S., R. E. Abercrombie, S. X. Chu, and T. Tai'ra (2024). The SCEC/USGS community stress drop validation study using the 2019 Ridgecrest earthquake sequence, *Seismica* **3,** no. 1, doi: 10.26443/seismica.v3i1.1009.

Bertero, M., D. Bindi, P. Boccacci, M. Cattaneo, C. Eva, and V. Lanza (1997). Application of the projected landweber method to the estimation of the source time function in seismology, *Inverse Probl.* **13,** 465–486.

Boatwright, J. (1980). A spectral theory for circular seismic sources; simple estimates of source dimension, dynamic stress drop, and radiated seismic energy, *Bull. Seismol. Soc. Am.* **70,** no. 1, 1–27, doi: 10.1785/BSSA0700010001.

Boatwright, J. (2007). The persistence of directivity in small earthquakes, *Bull. Seismol. Soc. Am.* **97,** no. 6, 1850–1861, doi: 10.1785/0120050228.

Brune, J. N. (1970). Tectonic stress and the spectra of seismic shear waves from earthquakes, *J. Geophys. Res.* **75,** no. 26, 4997–5009, doi: 10.1029/JB075i026p04997.

Burnham, K. P., and D. R. Anderson (2003). *Model Selection and Multimodel Inference: A Practical Information-Theoretic Approach*, Springer Science & Business Media, New York, New York, doi: 10.1007/b97636.

Calderoni, G., A. Rovelli, Y. Ben-Zion, and R. Di Giovambattista (2015). Along-strike rupture directivity of earthquakes of the 2009 L'Aquila, central Italy, seismic sequence, *Geophys. J. Int.* **203,** no. 1, 399–415, doi: 10.1093/gji/ggv275.

Charbonnier, P., L. Blanc-Féraud, G. Aubert, and M. Barlaud (1997). Deterministic edge-preserving regularization in computed imaging, *IEEE Trans. Image Process.* **6,** no. 2, 298–311.

Chatterjee, A., D. T. Trugman, G. Hirth, J. Lee, and V. C. Tsai (2024). High-frequency ground motions of earthquakes correlate with fault network complexity, *Geophys. Res. Lett.* **51,** e2024GL109418, doi: 10.1029/2024GL109418.

Chen, P., T. H. Jordan, and L. Zhao (2010). Resolving fault plane ambiguity for small earthquakes, *Geophys. J. Int.* **181,** 493–501, doi: 10.1111/j.1365-246x.2010.04515.

Cheng, Y., E. Hauksson, and Y. Ben-Zion (2023). Refined earthquake focal mechanism catalog for southern California derived with deep learning algorithms, *J. Geophys. Res.* **128,** e2022JB025975, doi: 10.1029/2022JB025975.

Chu, S., G. C. Beroza, and W. L. Ellsworth (2019). Source parameter variability of intermediate-depth earthquakes in Japanese subduction zones, *J. Geophys. Res.* **124,** 8704–8725, doi: 10.1029/2019JB017592.

Chu, S. X., V. C. Tsai, D. T. Trugman, and G. Hirth (2021). Fault interactions enhance high-frequency earthquake radiation, *Geophys. Res. Lett.* **48,** e2021GL095271, doi: 10.1029/2021GL095271.

Colavitti, L., G. Lanzano, S. Sgobba, F. Pacor, and F. Gallovič (2022). Empirical evidence of frequency-dependent directivity effects from small-to-moderate normal fault earthquakes in central Italy, *J. Geophys. Res.* **127,** no. 6, e2021JB023498, doi: 10.1029/2021JB023498.

Dempsey, D., and J. Suckale (2016). Collective properties of injection-induced earthquake sequences: 1. Model description and directivity bias, *J. Geophys. Res.* **121,** 3609–3637, doi: 10.1002/2015JB012550.

Folesky, J., J. Kummerow, S. A. Shapiro, M. Häring, and H. Asanuma (2016). Rupture directivity of fluid-induced microseismic events: Observations from an enhanced geothermal system, *J. Geophys. Res.* **121,** 8034–8047, doi: 10.1002/2016JB013078.

Gable, S., and Y. Huang (2024). Quantifying magnitude uncertainty of the 2019 Ridgecrest earthquake sequence through a sensitivity study of the relative magnitude method, *Bull. Seismol. Soc. Am.* doi: 10.1785/0120240126.

Hartzell, S. H. (1978). Earthquake aftershocks as Green's functions, *Geophys. Res. Lett.* **5,** 1–4, doi: 10.1029/GL005i001p00001.

Hirakawa, E., G. A. Parker, A. S. Baltay, and T. Hanks (2023). Rupture directivity of the 25 October 2022 5.1 alum rock earthquake, *Seism. Record* **3,** no. 2, 144–155, doi: 10.1785/0320230013.

Holmgren, J. M., G. M. Atkinson, and H. Ghofrani, (2019). Stress drops and directivity of induced earthquakes in the Western Canada Sedimentary Basin, *Bull. Seismol. Soc. Am.* **109,** no. 5, 1635–1652, doi: 10.1785/0120190035.

Hough, S. E. (1997). Empirical Green's function analysis: Taking the next step, *J. Geophys. Res.* **102,** no. B3, 5369–5384, doi: 10.1029/96JB03488.

Huber, P. J. (1964). Robust estimation of a location parameter, *Ann. Math. Stat.* **35,** no. 1, 73–101.

Imanishi, K., and W. L. Ellsworth (2006). Source scaling relationships of microearthquakes at Parkfield, CA, determined using the SAFOD pilot hole seismic array, in *Earthquakes: Radiated Energy and the Physics of Faulting*, R. Abercrombie, A. McGarr, G. Di Toro, and H. Kanamori (Editors), American Geophysical Union, Washington, D.C., doi: 10.1029/170GM10.

Kane, D. L., P. M. Shearer, B. Allmann, and F. L. Vernon (2013). Rupture directivity of small earthquakes at Parkfield, *J. Geophys. Res.* **118,** no. 1/10, doi: 10.1029/2012JB009675.

Kaneko, Y., and P. M. Shearer, (2014). Seismic source spectra and estimated stress drop derived from cohesive-zone models of circular subshear rupture, *Geophys. J. Int.* **197,** no. 2, 1002–1015, doi: 10.1093/gji/ggu030.

McGuire, J. J. (2004). Estimating finite source properties of small earthquake ruptures, *Bull. Seismol. Soc. Am.* **94,** no. 2, 377–393.

McGuire, J. J. (2017). A MATLAB toolbox for estimating the second moments of earthquake ruptures, *Seismol. Res. Lett.* **88,** no. 2A, 371–378, doi: 10.1785/0220160170.

McGuire, J. J., L. Zhao, and T. H. Jordan (2002). Predominance of unilateral rupture for a global catalog of large earthquakes, *Bull. Seismol. Soc. Am.* **92,** no. 8, 3309–3317.

Meng, H., J. J. McGuire, and Y. Ben-Zion (2020). Semiautomated estimates of directivity and related source properties of small to moderate southern California earthquakes using second seismic moments, *J. Geophys. Res.* **125,** e2019JB018566, doi: 10.1029/2019JB018566.

Mori, J., and A. Frankel (1990). Source parameters for small events associated with the 1986 North Palm Springs, California, earthquake determined using empirical Green functions, *Bull. Seismol. Soc. Am.* **80,** no. 2, 278–295, doi: 10.1785/BSSA0800020278.

Nevitt, J. M., B. A. Brooks, J. L. Hardebeck, and B. T. Aagaard (2023). 2019 M7.1 Ridgecrest earthquake slip distribution controlled by fault geometry inherited from Independence dike swarm, *Nat. Commun.* **14,** 1546, doi: 10.1038/s41467-023-36840-2.

Pennington, C. N., Q. Wu, X. Chen, and R. E. Abercrombie (2023). Quantifying rupture characteristics of microearthquakes in the Parkfield Area using a high-resolution borehole network, *Geophys. J. Int.* **233,** no. 3, 1772–1785, doi: 10.1093/gji/ggad023.

Prieto, G. A. (2022). The multitaper spectrum analysis package in python, *Seismol. Res. Lett.* doi: 10.1785/0220210332.

Prieto, G. A., B. Froment, C. Yu, P. Poli, and R. Abercrombie (2017). Earthquake rupture below the brittle-ductile transition in continental lithospheric mantle, *Sci. Adv.* **3,** e1602642, doi: 10.1126/sciadv.1602642.

Qiu, H., Y. Ben-Zion, R. Catchings, M. R. Goldman, A. A. Allam, and J. Steidl (2021). Seismic imaging of the Mw 7.1 Ridgecrest earthquake rupture zone from data recorded by dense linear arrays, *J. Geophys. Res.* **126,** e2021JB022043, doi: 10.1029/2021JB022043.

Ross, Z. E., and Y. Ben-Zion (2016). Toward reliable automated estimates of earthquake source properties from body wave spectra, *J. Geophys. Res.* **121,** 4390–4407, doi: 10.1002/2016JB013003.

Ross, Z. E., B. Idini, Z. Jia, O. L. Stephenson, M. Zhong, X. Wang, Z. Zhan, M. Simons, E. J. Fielding, S. H. Yun, *et al.* (2019). Hierarchical interlocked orthogonal faulting in the 2019 Ridgecrest earthquake sequence, *Science* **366,** 346–351, doi: 10.1126/science.aaz0109.

Ross, Z. E., D. T. Trugman, K. Azizzadenesheli, and A. Anandkumar (2020). Directivity modes of earthquake populations with unsupervised learning, *J. Geophys. Res.* **125,** e2019JB018299, doi: 10.1029/2019JB018299.

Seekins, L. C., and J. Boatwright (2010). Rupture directivity of moderate earthquakes in Northern California, *Bull. Seismol. Soc. Am.* **100,** no. 3, 1107–1119, doi: 10.1785/0120090161.

Shearer, P. M., G. A. Prieto, and E. Hauksson (2006). Comprehensive analysis of earthquake source spectra in southern California, *J. Geophys. Res.* **111,** no. B6, doi: 10.1029/2005JB003979.

Sheng, S., and L. Meng (2020). Stress field variation during the 2019 Ridgecrest earthquake sequence, *Geophys. Res. Lett.* **47,** e2020GL087722, doi: 10.1029/2020GL087722.

Spudich, P., J. R. Bayless, J. W. Baker, B. S. J. Chiou, B. Rowshandel, S. K. Shahi, and P. Somerville (2013). Final Report of the NGA-West2 directivity working group, *PEER Report 2013-09*, Pacific Earthquake Engineering Research Center, University of California, Berkeley, California.

Tomic, J., R. E. Abercrombie, and A. F. Do Nascimento (2009). Source parameters and rupture velocity of small M≤ 2.1 reservoir induced earthquakes, *Geophys. J. Int.* **179,** 1013–1023, doi: 10.1111/j.1365-246X.2009.04233.x.

Trugman, D. T. (2020). Stress-drop and source scaling of the 2019 Ridgecrest, California, earthquake sequence, *Bull. Seismol. Soc. Am.* **110,** no. 4, 1859–1871, doi: 10.1785/0120200009.

Trugman, D. T. (2022). Resolving differences in the rupture properties of M5 earthquakes in California using Bayesian source spectral analysis, *J. Geophys. Res.* **127,** e2021JB023526, doi: 10.1029/2021JB023526.

Van Houtte, C., and M. Denolle (2018). Improved model fitting for the empirical Green's function approach using hierarchical models, *J. Geophys. Res.* **123,** 2923–2942, doi: 10.1002/2017JB014943.

Wang, K., D. S. Dreger, E. Tinti, R. Bürgmann, and T. Taira (2020). Rupture process of the 2019 Ridgecrest, California M6.4 foreshock and M7.1 earthquake constrained by seismic and geodetic data, *Bull. Seismol. Soc. Am.* **110,** no. 4, 1603–1626, doi: 10.1785/0120200108.

White, M. C. A., H. Fang, R. D. Catchings, M. R. Goldman, J. H. Steidl, and Y. Ben-Zion (2021). Detailed traveltime tomography and seismic catalogue around the 2019 Mw7.1 Ridgecrest, California, earthquake using dense rapid-response seismic data, *Geophys. J. Int.* **227,** no. 1, 204–227, doi: 10.1093/gji/ggab224.

Xu, X., D. T. Sandwell, L. A. Ward, C. W. Milliner, B. R. Smith-Konter, P. Fang, and Y. Bock (2020). Surface deformation associated with fractures near the 2019 Ridgecrest earthquake sequence, *Science* **370,** 605–608, doi: 10.1126/science.abd1690.

Zhou, Z., M. Bianco, P. Gerstoft, and K. Olsen (2022). High-resolution imaging of complex shallow fault zones along the July 2019 Ridgecrest ruptures, *Geophys. Res. Lett.* **49,** e2021GL095024, doi: 10.1029/2021GL095024.

Manuscript received 1 July 2024